Sensors & Diagnostics

PAPER

View Article Online
View Journal

Cite this: DOI: 10.1039/d5sd00214a

A DSE–ESIPT-active organic luminogen for "turn-on" enantioselective recognition of chiral amino alcohols and selective hydrazine sensing

Aakash Venkatesan, [a] Baru Venkata Naga Sahithi, [b] Francis Joy, [a] Rupali Patel, [c] Aatika Nizam *[a] and Vasantha Veerappa Lakshmaiah *[b]

The development of dual-state emissive (DSE) organic luminogens has elevated the ease of recognition of various biological analytes, which demonstrates the multifaceted potential of dual-state emitters. Therefore, in this study, we synthesised a dual-state emissive excited-state intramolecular proton transfer (ESIPT)-based organic luminogen, (*E*)-4-(5-bromo-2-hydroxybenzylideneamino)-2,3-dimethyl-1-phenyl-1,2-dihydropyrazol-5-one (ANMB), exhibiting excitation-dependent phototunability with large Stokes shifts of 109 nm and 155 nm in both the solution and solid states, respectively, underscoring its potential as a biosensor. The metal-chelating ability of ANMB was investigated, revealing significant fluorescence quenching upon coordination with Cu^{2+} ions, leading to 96% reduction in emission intensity. The introduction of biological analytes, such as amino alcohols, enabled fluorescence recovery, where ANMB demonstrated enantioselective recognition: a single emission peak for the *S*-enantiomer and dual emission peaks for the *R*-enantiomer. Furthermore, ANMB demonstrated high selectivity for hydrazine detection in both the solution and solid states, with new emission bands observed at 411 nm and 432 nm, respectively, indicating a fluorescence shift from green to blue. Complementarily, ANMB was successfully applied for real-time imaging of hydrazine in food and plant samples, showcasing its practical adaptability. Additionally, *in silico* molecular docking studies were performed, revealing the potential therapeutic activity of ANMB against diarrheal targets. Overall, this work highlights the multifunctionality and tunability of DSE–ESIPT-based organic luminogens, positioning ANMB as a promising candidate for the selective recognition of biologically significant analytes in analytical and real-world contexts.

Received 25th November 2025,
Accepted 22nd January 2026

DOI: 10.1039/d5sd00214a

rsc.li/sensors

1. Introduction

Organic luminescent molecules have attracted the attention of researchers over the past few decades because of their ability to modify their optical signatures in response to external stimuli in the presence of specific substrates or variations in environmental physical parameters (pH, viscosity, temperature, pressure, polarity, *etc.*).[1] This enables their diverse practical applications in numerous fields, such as biological sciences,[2] pharmacology,[3] environmental sciences[4] and material sciences.[5] There are two main application categories for organic fluorescent chromophores. Most organic molecules exhibit strong fluorescence emission when solvated in organic or aqueous media owing to their significant radiative deactivation channels.[6] The chromophores demonstrating emission in solutions are used as fluorescent biomarkers for biomedical applications, including the imaging of cells,[7] cellular organelles,[8] tissues,[9] macromolecules,[10] and tumors.[11] However, their high emission in the solution phase is often accompanied by detrimental aggregation in the solid state. This enables a strong non-radiative deactivation process, a phenomenon known as aggregation-caused quenching (ACQ), which limits their practical applications in films and devices.[6] To avoid ACQ, Tang *et al.* proposed the concept of aggregation-induced emission (AIE), whereby molecular rotors in the chromophores facilitate non-radiative deactivation that causes fluorescence quenching in the solution state, whereas in the solid state, the restriction of the motion of the molecular rotors in the aggregated state activates radiative deactivation channels, resulting in strong fluorescence.[12] The applications of solid-state emissive organic fluorophores include data encryption (logic gates and anti-counterfeiting security inks)[13,14] and their use in devices such as organic

[a] *Department of Chemistry, Christ University, Bangalore-560029, India. E-mail: aatika.nizam@christuniversity.in*
[b] *Department of Life Sciences, Christ University, Bangalore-560029, India. E-mail: vasantha.vl@christuniversity.in*
[c] *Department of Physics and Electronics, Christ University, Bangalore-560029, India*

photovoltaics (OPVs),[15] organic light-emitting diodes (OLEDs)[16,17] and organic field effect transistors (OFETs).[18]

These materials have incentivized the research on molecules that exhibit fluorescence in both solution and solid states, which are popularized as dual-state emitters. Dual-state emissive (DSE) organic fluorophores were first reported by Tang *et al.* in 2015, and they have drawn a lot of interest as they allow for the use of a single fluorophore for a variety of applications, bridging the large functional gap between ACQ and AIE.[19] To construct a molecule with DSE properties, a delicate balance of planarity, rigidity, and solubility is required, which is challenging, particularly in sensing applications.[20] ESIPT-based molecules exhibit a range of capabilities, including reversible mechanochromism, aggregation-induced emission (AIE), ratiometric sensing, and anti-counterfeiting.[21] They exhibit photophysical properties owing to the phototautomerism of the excited normal species (N*) and tautomeric species (T*), resulting in dual emission peaks, corresponding to their enol (E*) and keto (K*) forms, respectively.[22] Thus, due to an easily apprehended proton transfer, this particular excited-state dynamics yields many advantageous characteristics, such as significant Stokes shifts, increased photostability, strong solid-state emission, and environment-sensitive optical properties.[6]

As a consequence, ESIPT-based DSE materials have emerged as attractive tools for the sensing of various biological analytes. Therefore, in this article, we present a DSE–ESIPT active organic luminogen, (*E*)-4-(5-bromo-2-hydroxybenzylideneamino)-2,3-dimethyl-1-phenyl-1,2-dihydropyrazol-5-one (ANMB), which exhibits chelation-induced quenching on complexation with Cu^{2+} ions, enabling ratiometric sensing of Cu^{2+} ions in the solution state. Furthermore, the retraction of the fluorescence was achieved by introducing phenylglycinol into the ANMB + Cu^{2+} system, attributed to the competitive affinity of phenylglycinol towards Cu^{2+} ions over ANMB, which triggers a "turn on" fluorescence emission. The selective detection of hydrazine in both solution and solid states was achieved through the formation of an imine bond between ANMB and hydrazine *via* the free carbonyl moiety in ANMB, leading to a hypsochromic shift in the emission spectrum from green to blue fluorescence. Henceforth, we put forth this ANMB organic luminogen as a multifaceted sensor for biological molecules. Additionally, *in silico* studies and bioimaging were performed to prove the potential adaptability of ESIPT hydrazone in multifaceted domains.

2. Experimental procedures

2.1 Materials and instrumentation

The experimental chemicals, such as 4-aminoantipyrine, 5-bromosalicylaldehyde, hydrazine hydrate, (*S*)-(+)-2-phenylglycinol and (*R*)-(−)-2-phenylglycinol, were purchased from Sigma Aldrich, and the solvents utilized were of spectroscopic grade and used without further purification. The absorption spectrum of the compounds was recorded using a Shimadzu UV1800 spectrophotometer in the range of 200–700 nm. Both solution and solid-state emission spectra of the compounds were recorded using a Shimadzu spectrofluorophotometer (RF-6000). The ^{1}H NMR spectrum was recorded in DMSO-d_6 using a Bruker Avance 400 MHz FT-NMR spectrometer.

2.2 Synthesis and characterisation of ANMB

The antipyrine-based sensor (**ANMB**) was prepared by a Schiff's base condensation reaction involving 4-aminoantipyrine (0.203 g, 1.0 mmol) and 5-bromosalicylaldehyde (0.201 g, 1.0 mmol) in ethanol for 6 h at 70 °C following a previously reported procedure.[23] A yellowish-orange color precipitate was procured on completion of the reaction and extracted using ethyl acetate. After equilibrium was reached, a rotary evaporator was employed to reduce the solvent volume, and a pure form of the product was obtained on slow evaporation. Techniques such as TLC and ^{1}H NMR revealed the product formation.

2.3 Preparation of fluorescent tags

Fluorescent tags were made from Whatman filter papers. The filter paper was dipped in a stock solution of **ANMB** (1.5×10^{-3} M) prepared in DMF-Tris buffer (9/1, v/v, pH 7.4) and dried in a hot air oven for 3 h to obtain fluorescent tags,[24] which exhibited lime green fluorescence under UV light (365 nm). These fluorescent tags were used to investigate the solid-state response of **ANMB** towards various hydrazine derivatives.

2.4 Molecular docking studies

The computational docking of **ANMB** was performed using AutoDock Vina as an extension in UCSF Chimera.6-7. The protein *Mus musculus* opioid receptors (ORs), including muOR (μOR) and deltaOR (δOR), and the M3 muscarinic acetylcholine receptor structures were retrieved from RCSB Protein DataBank (PDB) (http://www.rcsb.org/pdb), PDB-ID 5C1M, 4EJ4 and 4U14. The proteins and the ligand were prepared following the procedures in a published work.[25] Discovery Studio Visualizer v.21.1.0.20298 was used to create the 2D diagrams.

2.5 ADME prediction

In silico ADME analysis was conducted using SwissADME to investigate the physicochemical properties, lipophilicity, water solubility, pharmacokinetics, and drug likeness of the materials.

2.6 Latent fingerprint analysis

A latent fingerprint study was performed using fingerprints voluntarily provided by an adult participant who provided informed consent. No personal or identifiable information was collected. The hands were washed thoroughly with soap

and water, after which the fingers were directed to gently touch naturally oily regions of the face (nose and forehead) and then pressed onto glass substrates under ambient conditions for practical accessibility. To develop the latent fingerprints using the organic luminogen, a small amount of the powder was applied to the imprinted substrates using a soft brush, and excess material was removed by a gentle air flow. Optical images of the latent fingerprints before and after probe treatment were recorded using a mobile phone under UV illumination (365 nm). The experiment was repeated three times, yielding consistent visualization results.[26]

3. Results and discussions

3.1 Synthesis of ANMB

(*E*)-4-(5-Bromo-2-hydroxybenzylideneamino)-2,3-dimethyl-1-phenyl-1,2-dihydropyrazol-5-one (**ANMB**) was synthesized at 70 °C in ethanol and subsequently refluxed for 6 h to afford the product in 98% yield (Scheme S1, SI). ^{1}H NMR analysis confirmed the product formation (Fig. S1, SI). ^{1}H NMR (δ, ppm): 12.73 (OH, s); 9.65 (HC═N, s); 7.74–7.73 (1H, d); 7.56–7.53 (2H, t); 7.44–7.37 (4H, m); 6.89–6.87 (1H, d); 3.22 (3H, s); 2.50–2.49 (3H, t).

3.2 Investigation of optical properties of ANMB

The optical response of ESIPT-based molecules can be significantly influenced by various external stimuli, such as changes in solvent polarity, varying water fractions, and the coordination of various guest molecules and metal ions. In the present study, **ANMB** demonstrated an active excited state intramolecular proton transfer (ESIPT) due to the hydroxy group of the salicylaldehyde moiety and the imino nitrogen in both the solution and solid states.

3.2.1. Excitation-dependent emission characteristics of ANMB. To evaluate the excitation-dependent properties of **ANMB**, serial excitation-emission spectral measurements

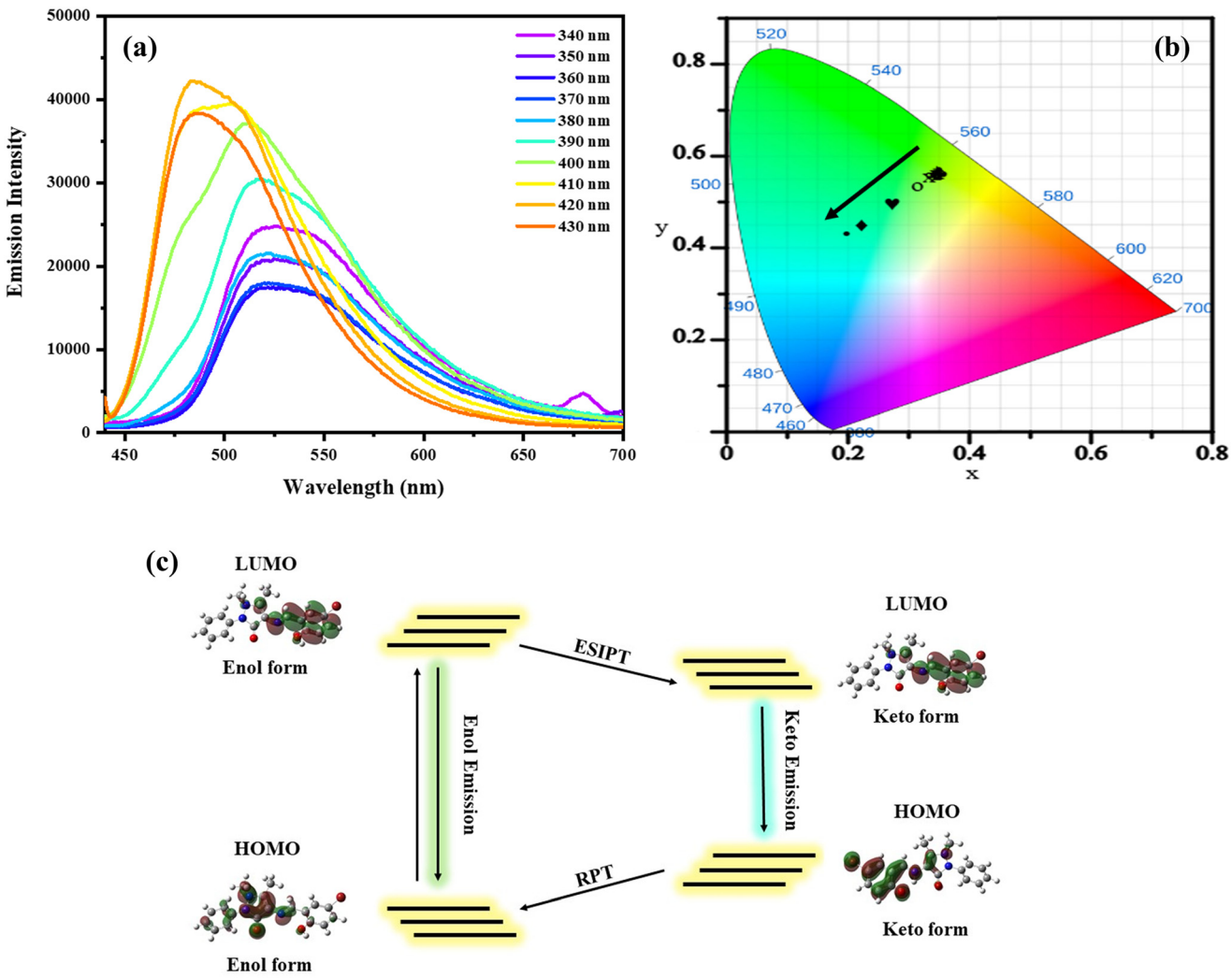

Fig. 1 (a) Emission spectra (ANMB (c = 36.5 μM); DMF/H_2O (9 : 1, v/v) at pH 7.4; slit width = 5 nm/5 nm; measured at room temperature). (b) CIE plot of ANMB under varying excitation wavelengths. (c) Proposed DSE-ESIPT mechanism for ANMB.

were carried out by subjecting the probe to various excitation wavelengths ranging from 340 nm to 430 nm (Fig. 1a). Upon excitation at 400 nm, a dual-emission intensity peak, shouldered at 477 nm and 510 nm, was observed, due to the phototautomerization process, in which the distinctive peaks were ascribed to the keto and enol forms of **ANMB**, respectively. A noticeable hypsochromic shift of about 34 nm was observed as the excitation wavelength increased, and the maximum emission intensity was observed at an excitation wavelength of 430 nm, beyond which the intensity peak diminished on further increasing the excitation wavelength, revealing that the relative intensity peak changes with the excitation wavelength. As a significant hypsochromic shift is observed on varying the excitation wavelengths, to comprehend the color-switching response of **ANMB**, a CIE coordinate diagram was developed (Fig. 1b). The analysis disclosed a transition from green to blue upon methodically varying the excitation wavelengths.

Thus, the heterogeneous properties of **ANMB** can be attributed to the photoisomerization process. Excitation at wavelengths greater than 400 nm resulted in a pronounced blue shift in the emission peak, suggesting the conversion of the enol tautomer to the keto form. The divergence of the keto and enol forms is due to the interaction between the hydroxy group of the salicylaldehyde moiety and the imine nitrogen in the probe. This evidence alludes to the attainable ESIPT mechanism for ANMB and illustrates the proposed emission process (Fig. 1c).

3.2.2. Solvochromic characteristics of ANMB. The solubility and change in the photophysical properties of **ANMB** are evaluated using its emission (Fig. 2a) and absorption spectra (Fig. 2b) while varying the solvent polarity (DMSO, DMF, THF, EA, chloroform, EtOH, and MeOH). In all the solvents tested, **ANMB** showed a comparable absorption peak at 356–364 nm, which indicates that the electronic structure of the **ANMB** is independent of the solvent environment. Minimal intramolecular charge transfer occurs, indicating that **ANMB** is a highly rigid fluorophore. Similarly, the emission spectra of **ANMB** revealed a significant amount of fluorescence in almost all solvents, with shoulder peaks observed at 510–526 nm, but a noticeable hypsochromic shift of 74–82 nm was observed in highly polar solvents. This suggests that a possible hydrogen bonding or proton transfer in the excited state reduces the charge separation, making the excited state less stabilized and enabling a hypsochromic shift. This observation reveals that **ANMB** is dependent on the solvent polarity (Fig. 2c). This highlights the ESIPT mechanism exhibited by **ANMB**.

The compiled photophysical data of **ANMB** under various solvent-polarity conditions (Table S1 and Fig. S2, SI) are

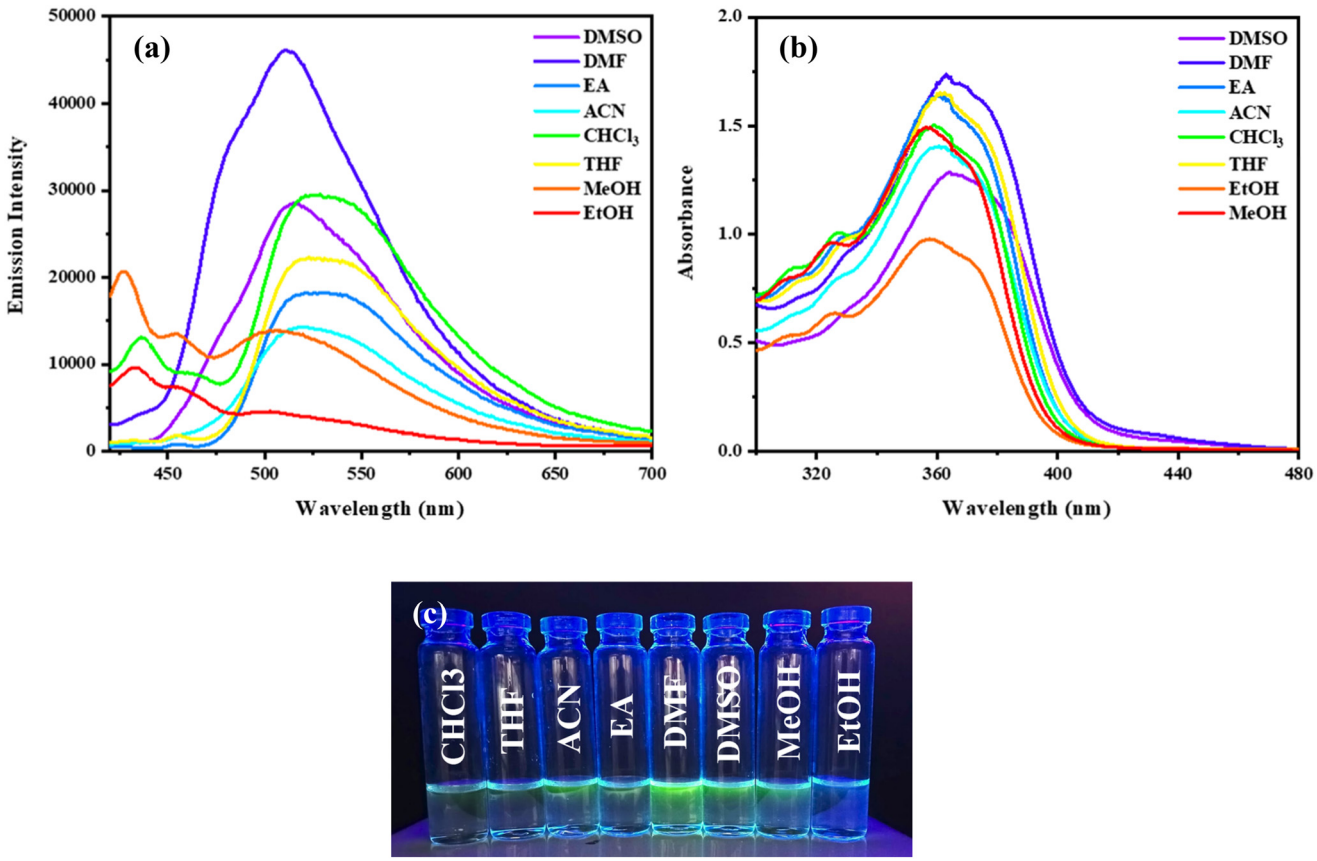

Fig. 2 (a) Emission spectra (ANMB (c = 36.5 μM); solvent/H_2O (9 : 1, v/v) at pH 7.4; λ_{ex} = 390 nm; slit width = 5 nm/5 nm; measured at room temperature). (b) Absorption spectra of ANMB in various solvents. (c) Photographic image of ANMB in various solvents.

calculated, and the lowest quantum yield was observed in MeOH (φ = 0.0024). This can be attributed to the high polarity of the solvent that restricts the formation of intramolecular hydrogen bonds, which inhibits proton transfer in the **ANMB** system. The highest quantum yield was noticed in DMSO (φ = 0.0136) and DMF (φ = 0.0141). This can be ascribed to the polar aprotic and viscous nature of the solvents that restrict the rotation and promote the efficient transfer of intramolecular protons in the **ANMB** system, thereby stabilizing the bonds in the excited state. Therefore, based on the quantum yield value, DMF was selected as the optimal solvent for all of the studies conducted.

3.2.3. Stokes shift of ANMB in the solution and solid states. The emission and absorption spectra were examined in both the solid and solution states (Fig. 3a and b) to determine the Stokes shift values. In the solid state, an emission peak shouldered at 527 nm and an absorption maximum shouldered at 372 nm were obtained, while in the solution state, an emission peak shouldered at 512 nm and an absorption maximum shouldered at 403 nm were obtained. Significant Stokes shifts of around 109 nm in the solution state and 155 nm in the solid state were obtained when the aforementioned spectrum was analyzed. This shift minimizes measurement oversights and affirms the highly reliable sensing performance of **ANMB** by reducing spectral overlap and backscattering.

3.2.4. Aggregation-induced quenching characteristics of ANMB. To assess the aggregation-induced quenching properties of **ANMB**, the emission spectra were recorded while varying the water fractions (wf) in DMF from 0% to 90% (Fig. S3, SI). Initially, the fluorescence emission increased negligibly at 10% wf with an emission peak shoulder at 513 nm. Upon increasing the wf subsequently from 10% to 90%, there was a gradual decrease in the intensity of the emission peak at 513 nm. This was attributed to the development of an ordered assembly of emissive crystalline aggregates that led to the concentration quenching effect, validating the ACQ behavior of **ANMB**. A visible change in the photophysical property of **ANMB** upon varying the water fractions was observed under UV light (365 nm).

3.2.5. Metal-chelation-induced quenching characteristics of ANMB. To understand the metal-chelation-induced fluorescence quenching of **ANMB**, various metal ion solutions, such as Sn^{2+}, Ni^{2+}, Mg^{2+}, Hg^{2+}, Cu^{2+}, Co^{2+}, Cd^{2+}, Al^{3+}, and Fe^{3+}, were prepared. After adding each metal solution in a specified volume to the **ANMB**, the emission spectrum was recorded (Fig. 4a). The evaluation of the spectral analysis divulged that there was a noticeable quenching of fluorescence emission upon the chelation with the metal ions. When compared with the fluorescence emission intensity of **ANMB**, Cu^{2+} and Fe^{3+} ions exhibited remarkable fluorescence quenching efficiencies of 96% and 83%. However, Ni^{2+}, Co^{2+}, Hg^{2+}, Al^{3+}, and Cd^{2+} induced an approximate reduction of 50%, while Sn^{2+} and Mg^{2+} induced no significant fluorescence quenching, with a reduction of up to 15%. The data showed that the fluorescence quenching nature of **ANMB** was extremely sensitive to Cu^{2+} ions (Fig. 4b). This can be ascribed to the electron or energy transfer to Cu^{2+}, which causes the excited fluorophore to exhibit rapid non-radiative decay, due to the inherent paramagnetic character of Cu^{2+} ions. An interference study was carried out to evaluate the effect of other metal ions on the quenching nature of **ANMB** towards Cu^{2+} ions (Fig. S4, SI), which revealed that no significant changes were observed on the addition of other metal ions to the **ANMB**–Cu^{2+} system, proving the selectivity and sensitivity of **ANMB** towards Cu^{2+} ions.

3.2.5.1. Absorption spectral studies. To examine the Cu^{2+}-ion estimation by **ANMB**, the absorption spectra of **ANMB** were recorded upon adding the Cu^{2+} ions (Fig. 5a). Ratiometric sensing of Cu^{2+} ions was achieved, characterized by the initial absorption peak of **ANMB** centered at 360 nm.

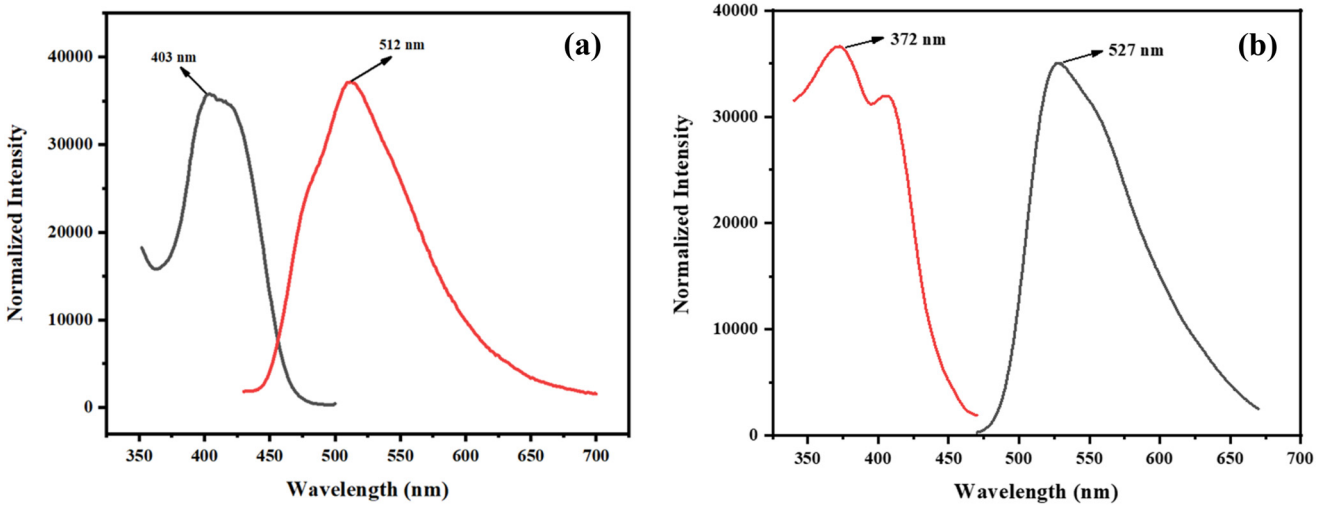

Fig. 3 Stokes shift determination in the (a) solution state (ANMB (c = 36.5 μM); DMF/H_2O (9 : 1, v/v) at pH 7.4; λ_{ex} = 390 nm; slit width = 5 nm/5 nm; measured at room temperature) and (b) solid state.

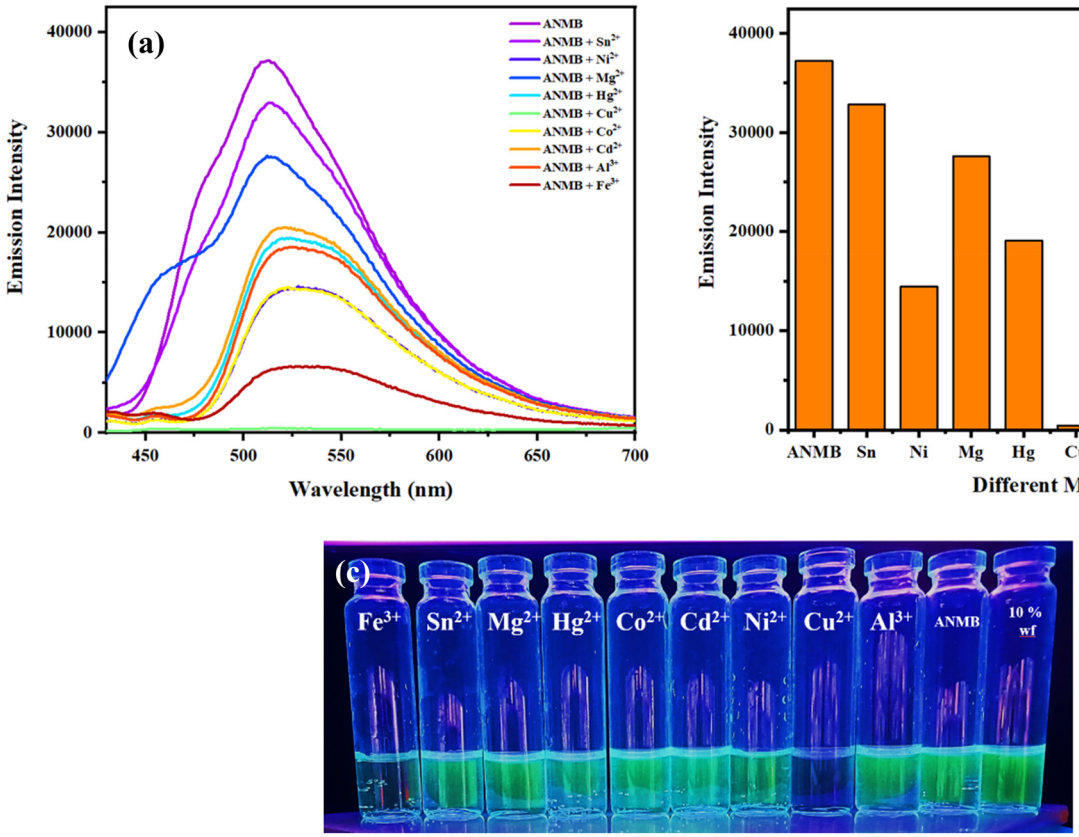

Fig. 4 (a) Emission spectra of ANMB with various metal ions (ANMB (c = 36.5 μM); DMF/H_2O (9 : 1, v/v) at pH 7.4; λ_{ex} = 390 nm; slit width = 5 nm/5 nm; measured at room temperature). (b) Histogram of ANMB quenching with various metal ions. (c) Photographic image of ANMB with various metal ions under UV light (365 nm).

Upon increasing the concentration of Cu^{2+} ions, the absorption peak intensity at 360 nm decreased drastically and was accompanied by a bathochromic shift of 20 nm. Subsequently, a new absorption peak at 420 nm emerged, indicating the color change to yellow upon increasing the Cu^{2+}-ion concentration. To estimate the limit of detection (LOD) and limit of quantification (LOQ), a linear plot between A_{420}/A_{360} and the Cu^{2+}-ion concentration was drawn (Fig. 5c). The LOD and LOQ were found to be 5.91 μM and 17.92 μM, respectively.

3.2.5.2. Photoluminescence spectral studies. To assess the photophysical response of **ANMB** towards Cu^{2+} ions, the Cu^{2+}-ion solution was added to **ANMB** incrementally, which induced significant fluorescence quenching, as indicated by the emission peak at 509 nm (Fig. 5b). Therefore, an emission titration of **ANMB** was performed by introducing Cu^{2+} ions. This induced the sequential quenching of the fluorescence intensity, and complete quenching of fluorescence was noticed after the addition of 26 equiv of Cu^{2+} ions. A linear plot of the emission intensity *vs.* concentration of Cu^{2+} ions was utilized for the estimation of LOD and LOQ (Fig. 5d), which were found to be 3.11 μM and 9.41 μM, respectively.

*3.2.5.3. Proposed mechanism for **ANMB** and Cu^{2+}-ion chelation.* Job's plot and Benesi–Hildebrand (BH) plot analyses were performed to gain insight into the binding interaction between **ANMB** and Cu^{2+} (Fig. 6a and b). The results suggest the possibility of a higher-order association, consistent with a 1 : 2 (Cu^{2+} : **ANMB**) binding model. The observed non-linearity in the BH plot further supports deviation from a simple 1 : 1 binding interaction, although definitive stoichiometry determination requires independent confirmation. As per the regulation of the U.S. Environmental Protection Agency, the allowed concentration of copper ions in drinking water is 20 μM.[27] Therefore, in the presence of the **ANMB** probe, the naked eye can be adopted to assess whether the level of copper ions has exceeded the standard limit in actual samples. The observed fluorescence quenching can be attributed to electron or energy transfer from the excited fluorophore to Cu^{2+}, which induces rapid non-radiative decay due to the inherent paramagnetic nature of Cu^{2+} ions. This interaction is likely to perturb the ESIPT and photo-induced electron transfer (PET) processes of the probe, leading to effective fluorescence quenching. Information from Job's plot suggested the formation of a 1 : 2 stoichiometry complex; aided by literature reports, a plausible mechanism and complex structure were suggested (Fig. 6c and d).

3.2.5.4. Mathematical model studies. Mathematical modelling studies, such as Stern–Volmer plot analysis, were carried out to assess the fluorescence quenching efficiency of the Cu^{2+} ion upon addition to the **ANMB** solution (Fig. 7a).

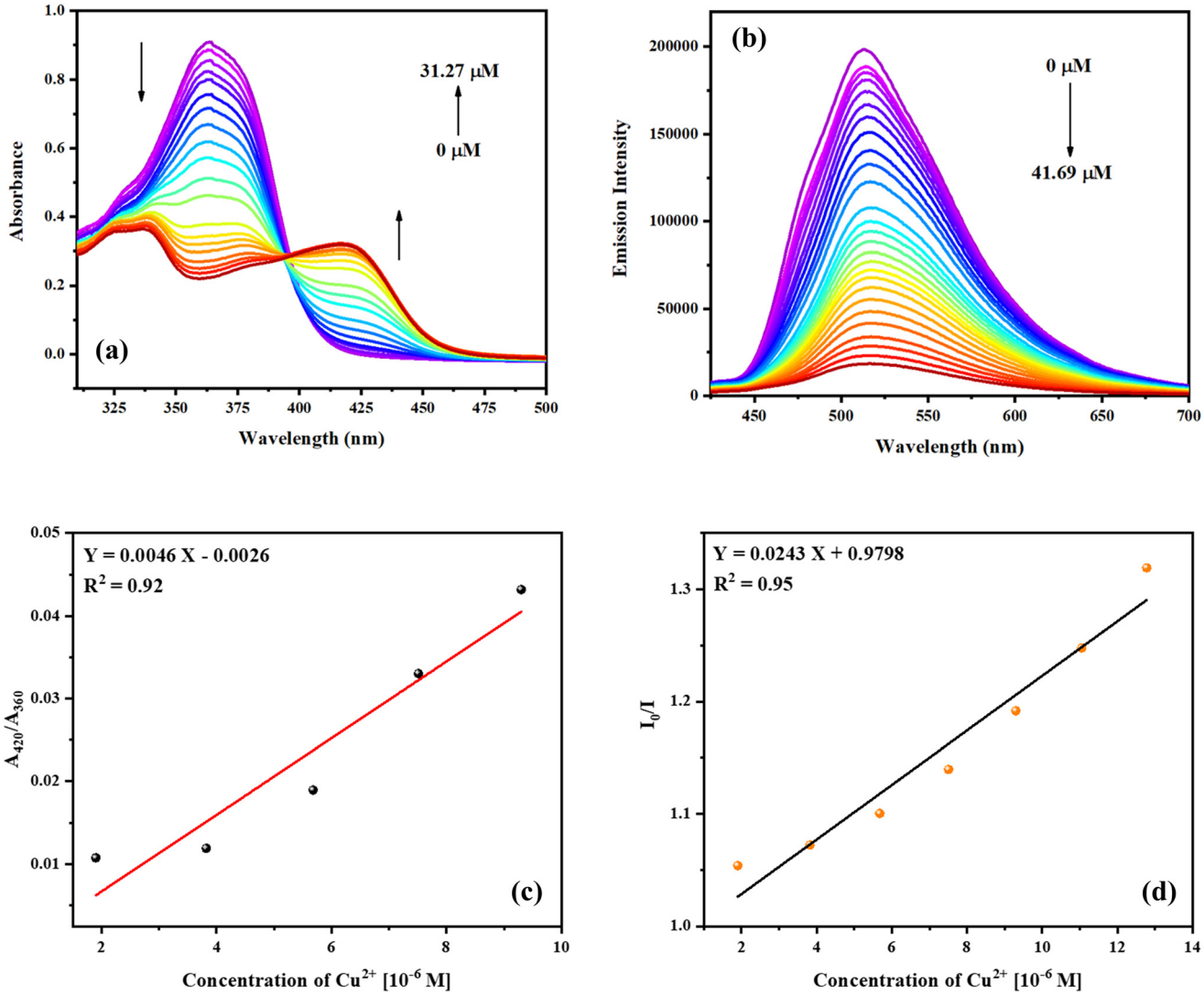

Fig. 5 Titration studies of ANMB with Cu^{2+} ions: (a) absorption spectra and (b) emission spectra. Linear plot for the (c) absorption spectra and (d) emission spectra (ANMB (c = 36.5 μM); DMF/H_2O (9 : 1, v/v) at pH 7.4; λ_{ex} = 390 nm; slit width = 5 nm/5 nm; measured at room temperature).

The results revealed that at higher concentrations of Cu^{2+}, a discernible nonlinear behaviour with curvature is observed. This anomalous behaviour is well established in other stable copper complex systems based on molecular quenchers, which should thus provide a linear curve. In the present instance, however, the upward curve astonishingly changed to a linear rise at relatively high Cu^{2+} concentrations, subsequently producing a plateau that denotes equilibrium at higher concentrations. The product, $\tau_f\ k_q$, from the slope was found utilizing Stern–Volmer eqn (1) and (2) and the plot (Fig. 7b).

$$\frac{I_0}{I_q} = 1 + \tau_f k_Q [Q], \quad (1)$$

$$\frac{I_0}{I_q} = 1 = \tau_f k_Q [Q], \quad (2)$$

where I_0 and I_q are the fluorescent intensity without and with a quencher, respectively; K_q is the quenching constant, and τ_f is the fluorescence lifetime. The value of $\tau_f\ k_q$ was determined to be 0.02431 $mol^{-1}\ s^{-1}$.

The binding interaction between Cu^{2+} and **ANMB** was analyzed (Fig. S5, SI) using a 1 : 2 binding model, yielding binding constants of K_{11} = 5.14 M^{-1} and K_{21} = 3.44 × 10^6 M^{-1}. The error estimates for K_{11} and K_{21} were 13.89% and 1.03%, respectively. The significantly higher K_{21} value suggests a positive cooperativity effect, where the second ligand binds with much stronger affinity than the first. The model fitting was evaluated using residual analysis and sum of squared residuals (SSR = 1.44 × 10^7), indicating a reasonable fit to the experimental data.

3.2.5.5. Theoretical studies. The structures of ANMB in its enol (ANMB_enol) and keto (ANMB_keto) forms, along with the Cu^{2+} complex (ANMB_Cu^{2+}), were optimized using DFT at the B3LYP functional level. For the free probe forms (ANMB_enol and ANMB_keto), the 6-311G(d,p) basis set was employed, while the LANL2DZ basis set was used for the

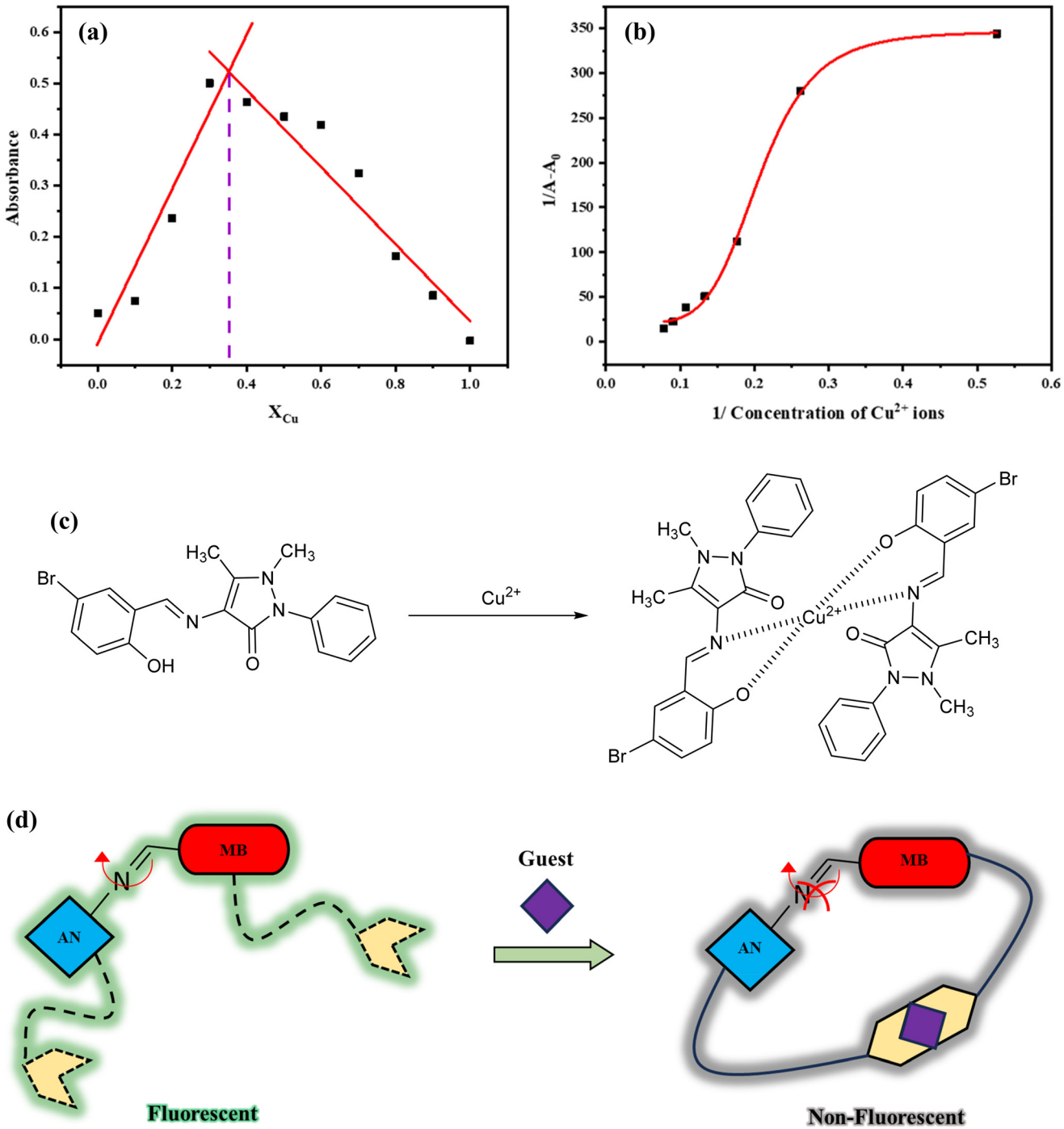

Fig. 6 (a) Jobs plot, (b) BH plot, (c) structure of the ANMB–Cu^{2+} complex and (d) plausible mechanism of fluorescence quenching.

Cu^{2+}-containing complex. A comparative analysis of the optimized geometrical parameters and energy profiles of ANMB and its metal complex (Fig. 8a) provides insights into the response mechanism of the probe toward metal-ion binding. The orbital energies of the HOMO of ANMB_enol are primarily localized in the salicylaldehyde region, and the LUMO is localized over the pyrazolone ring of the antipyrine molecule. In contrast, both the HOMO and LUMO of the ANMB_keto are localized over the salicylaldehyde region, extending into the pyrazolone unit, suggesting a more symmetric electron distribution. Interestingly, the ANMB_Cu^{2+} complex exhibits similar orbital localization to that of the keto form, supporting the hypothesis that chelation is favoured in the keto tautomeric state. This electronic reorganization implies that ANMB_enol, due to the spatial separation of frontier orbitals, is less effective in coordinating Cu^{2+} ions, possibly leading to partial or weak binding. Conversely, in the keto form, the HOMO–LUMO

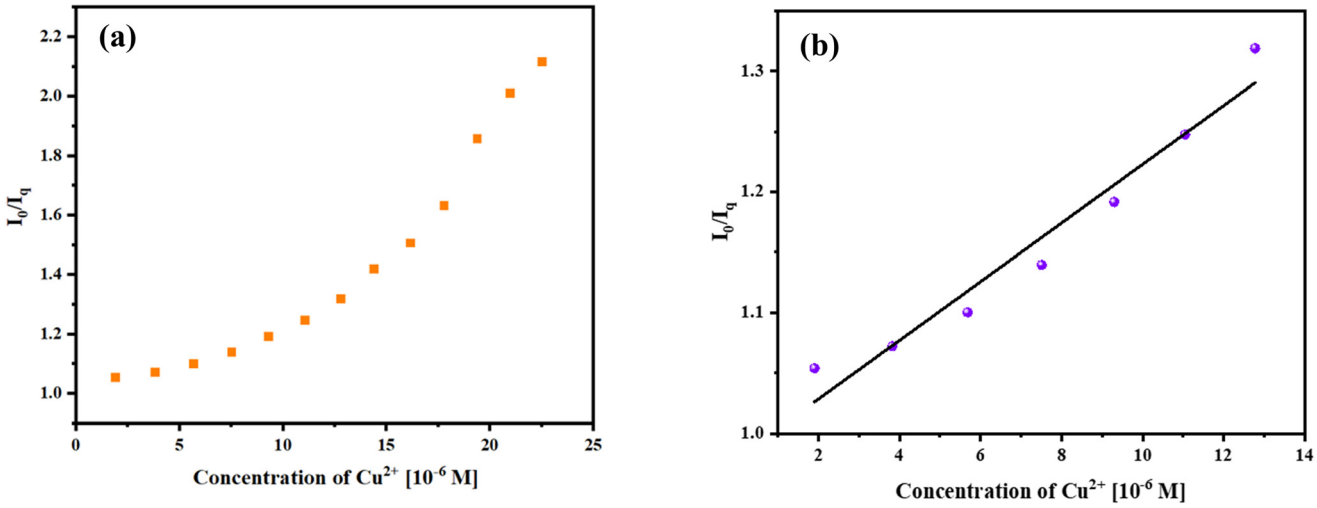

Fig. 7 (a) Stern–Volmer plot and (b) linear plot.

density is localized in the region encompassing key donor atoms, which includes the phenolate oxygen (O^-), imine nitrogen (N), and carbonyl oxygen of the pyrazolone ring (C═O), enabling strong and complete chelation of Cu^{2+} ions. Therefore, the observed orbital behaviour aligns with the structural transition from enol to keto and correlates with the enhanced metal-binding capability of the probe in its keto form. Based on this, the Cu^{2+} ions coordinate with two molecules of **ANMB** through a six-coordination arrangement with two phenolate oxygen (O^-), two imine nitrogen (N), and two carbonyl oxygen of the pyrazolone ring (C═O), adopting a distorted octahedral geometry. Additionally, the reduction of the HOMO–LUMO energy gap upon chelation was attributed to the increased conjugation, electron delocalization, and orbital interaction in the presence of the metal ion, which facilitates full chelation and significantly modifies the electronic structure of the probe.

The electrostatic potential (ESP) plot was generated to visualize the distribution of electrostatic charge over the molecular surfaces of ANMB in its different forms. In ANMB_enol, the ESP map revealed a localized region of negative potential concentrated around the hydroxyl (OH) group of the salicylaldehyde moiety, indicating limited electron delocalization. In contrast, the ANMB_keto exhibited a more delocalized negative electrostatic potential extending across the phenolate oxygen (O^-), imine nitrogen (N), and carbonyl oxygen (C═O) of the pyrazolone ring. This delocalization suggests a more conjugated system in the keto form, which enhances its ability to coordinate with metal ions. Upon complexation with Cu^{2+} ions, the ESP plot of the resulting ANMB_Cu^{2+} complex showed a significant neutralization of the negative potential, and the electrostatic distribution became more uniform across the entire molecule. This transformation supports the formation of a stable, fully chelated complex, involving two ANMB ligands coordinating with a single Cu^{2+} ion. The loss of localized negative regions further confirms that the key donor atoms (phenolate O^-, imine N, and pyrazolone C═O) are involved in complete chelation, stabilizing the metal center and validating the binding mechanism suggested by the electronic structure analysis.

3.3 Sensing of biological analytes and biological activity

Upon investigating the multifaceted properties of ANMB, we tested its sensing performance towards biological analytes, such as (*S*)-(+)-2-phenylglycinol, (*R*)-(−)-2-phenylglycinol, and hydrazine, which exhibit selectively enhanced fluorescence responses.

3.3.1. Amino alcohol response towards ANMB. It is generally known that because amino and hydroxyl groups are available for coordination, amino alcohols have a considerable affinity for Cu^{2+}. Thus, it was assumed that adding amino alcohols to the **ANMB**–Cu^{2+} solution would enable Cu^{2+} to bind to amino alcohols competitively. This would result in the restitution of fluorescence and a "turn-on" fluorescent signal, as the free **ANMB** would reappear.

3.3.1.1. Photoluminescence studies. The **ANMB**-based amino alcohol chemosensor's potential was examined using the emission spectrum. The optimized condition, which included 50 μL of **ANMB** stock solution and 25 μM of Cu^{2+}, was applied after the trials. For detection under the nearly neutral state for compatibility with biological systems, a pH of 7.4 was maintained. The fluorescence recovery was observed as the concentration of (*S*)-(+)-2-phenylglycinol increased from 0 to 64.71 μM, with an emission peak shouldered at 497 nm, along with a hypochromic shift of roughly 14 nm (Fig. 9a). Additionally, fluorescence recovery was observed as the concentration of (*R*)-(−)-2-phenylglycinol increased from 0 to 40.25 μM, with a dual emission peak shouldered at 464 and 502 nm (Fig. 9c), which enables **ANMB** to outperform as an enantioselective sensor of amino alcohols. No discernible change in the fluorescence emission was seen upon further addition, which indicates the equilibrium point of the

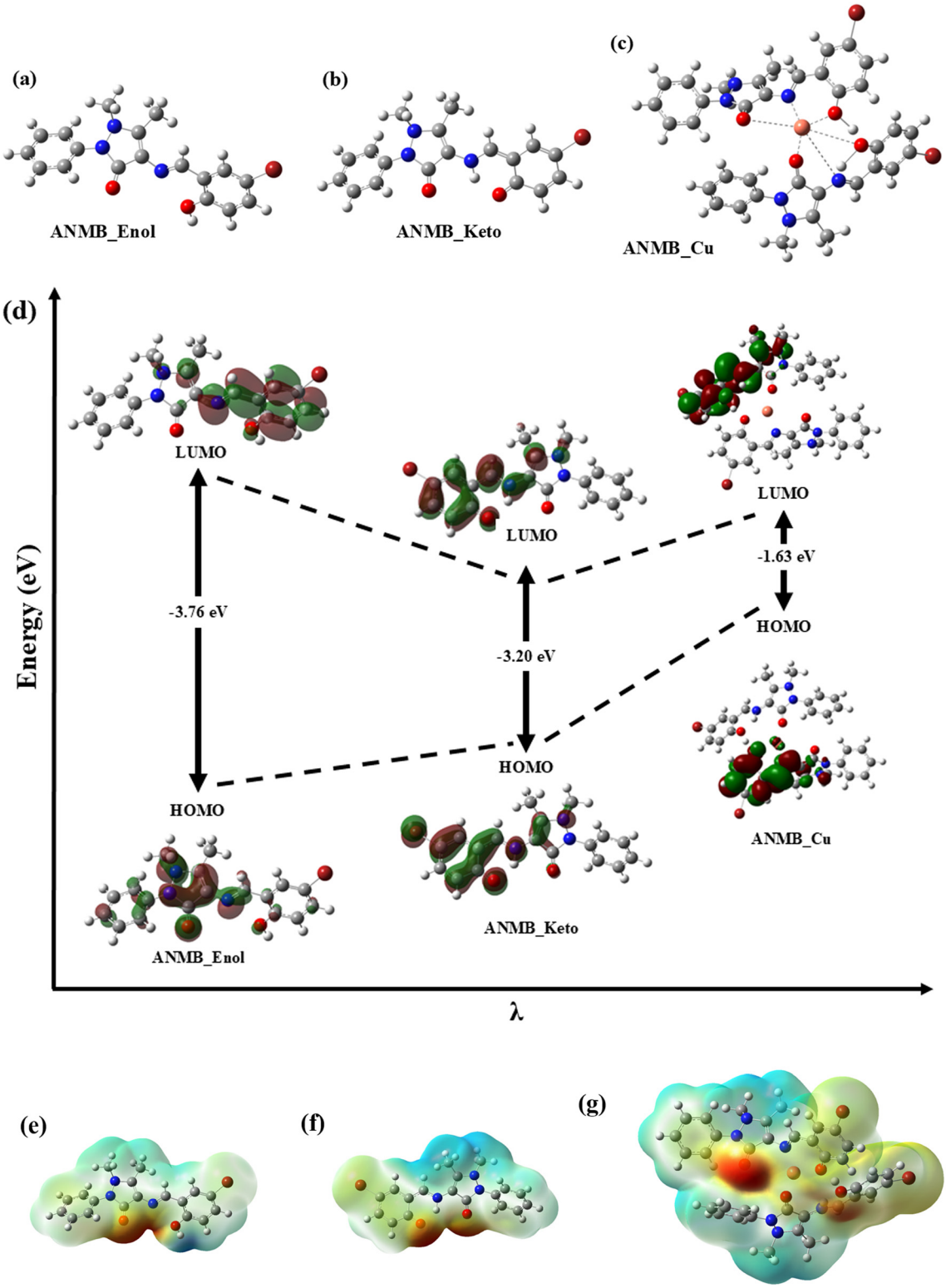

Fig. 8 (a) Optimized geometries of ANMB_X in the (a) enol form, (b) keto form and (c) Cu-coordinated form. (d) Energy profile of HOMO and LUMO for the optimized geometries of ANMB_X. ESP plot for the optimized geometries of ANMB_X in the (e) enol form, (f) keto form and (g) Cu-coordinated form.

chemosensor towards amino alcohols. The probe may exhibit this behaviour due to simultaneous association and dissociation with the metal ion. Consequently, the probe's free form is present at all times throughout the reaction. This anomalous fluorescence recovery behaviour of the **ANMB**–Cu^{2+} system is due to the stabilisation of both conformers or

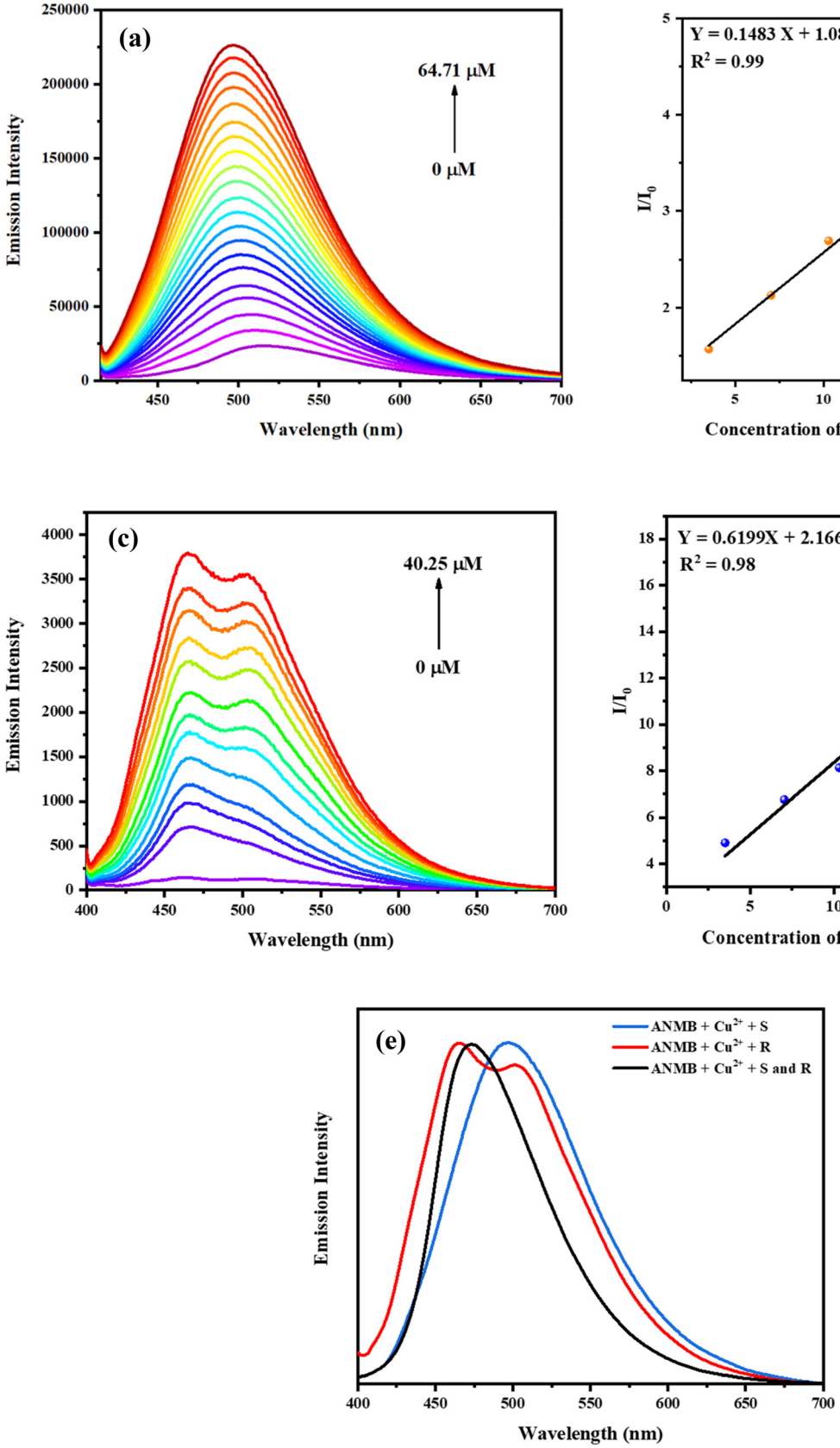

Fig. 9 (a) Emission titration spectra and (b) linear plot of ANMB–Cu^{2+} with (*S*)-(+)-2-phenylglycinol. (c) Emission titration spectra and (d) linear plot of ANMB–Cu^{2+} with (*R*)-(–)-2-phenylglycinol. (e) Emission spectrum of ANMB with an equimolar mixture of (*R*)-(–) and (*S*)-(+)-2-phenylglycinol (ANMB (c = 36.5 μM); Cu^{2+} (c = 25 μM); DMF/H_2O (9 : 1, v/v) at pH 7.4; λ_{ex} = 390 nm; slit width = 5 nm/5 nm; measured at room temperature).

electronic states of **ANMB** by the *R* enantiomer, thereby exhibiting two distinct emission peaks, each associated with its corresponding electronic state. Contrary to that for the *R* enantiomer, a single emission peak was observed in the case of the *S* enantiomer, which was attributed to the conformation or steric hindrance that prevents ESIPT, allowing only normal emission. The LOD and LOQ were estimated using a linear plot of emission intensity *vs.* (*S*)-(+)-2-phenylglycinol and (*R*)-(−)-2-phenylglycinol concentration (Fig. 9b and d), and the results showed that they were 1.13 μM and 3.42 μM for (*S*)-(+)-2-phenylglycinol and 3.32 μM and 10.07 μM for (*R*)-(−)-2-phenylglycinol, respectively. The bindfit model studies (Fig. S6, SI) also suggested the strong interaction between the **ANMB**–Cu^{2+} system and (*S*)-(+)-2-phenylglycinol and (*R*)-(−)-2-phenylglycinol. Furthermore, fluorescence measurements performed with a mixture containing both *R* and *S* enantiomers (Fig. 9e) produced an emission spectrum distinct from those of the individual enantiomers, suggesting competitive binding and differential interaction within the chiral environment of the **ANMB**–Cu^{2+} ensemble. All experiments were conducted under identical conditions, including solvent composition, Cu^{2+} concentration, and total analyte concentration, minimizing the possibility of concentration- or aggregation-induced artifacts.

3.3.2. Hydrazine response towards ANMB

3.3.2.1. Photoluminescence studies. Emission spectra were measured to investigate the selective sensing of hydrazine in solution (Fig. 10a). On incremental addition of hydrazine to the probe solution, new dual peaks appeared at 411 and 432 nm, and the probe emission peak intensity at 520 nm increased, displaying a blueish green fluorescence that indicates the partial interaction of **ANMB** and hydrazine. This behaviour was observed until the hydrazine concentration reached 0.73 mM, and on further addition of hydrazine, the emission peak at 520 nm began to drop, and

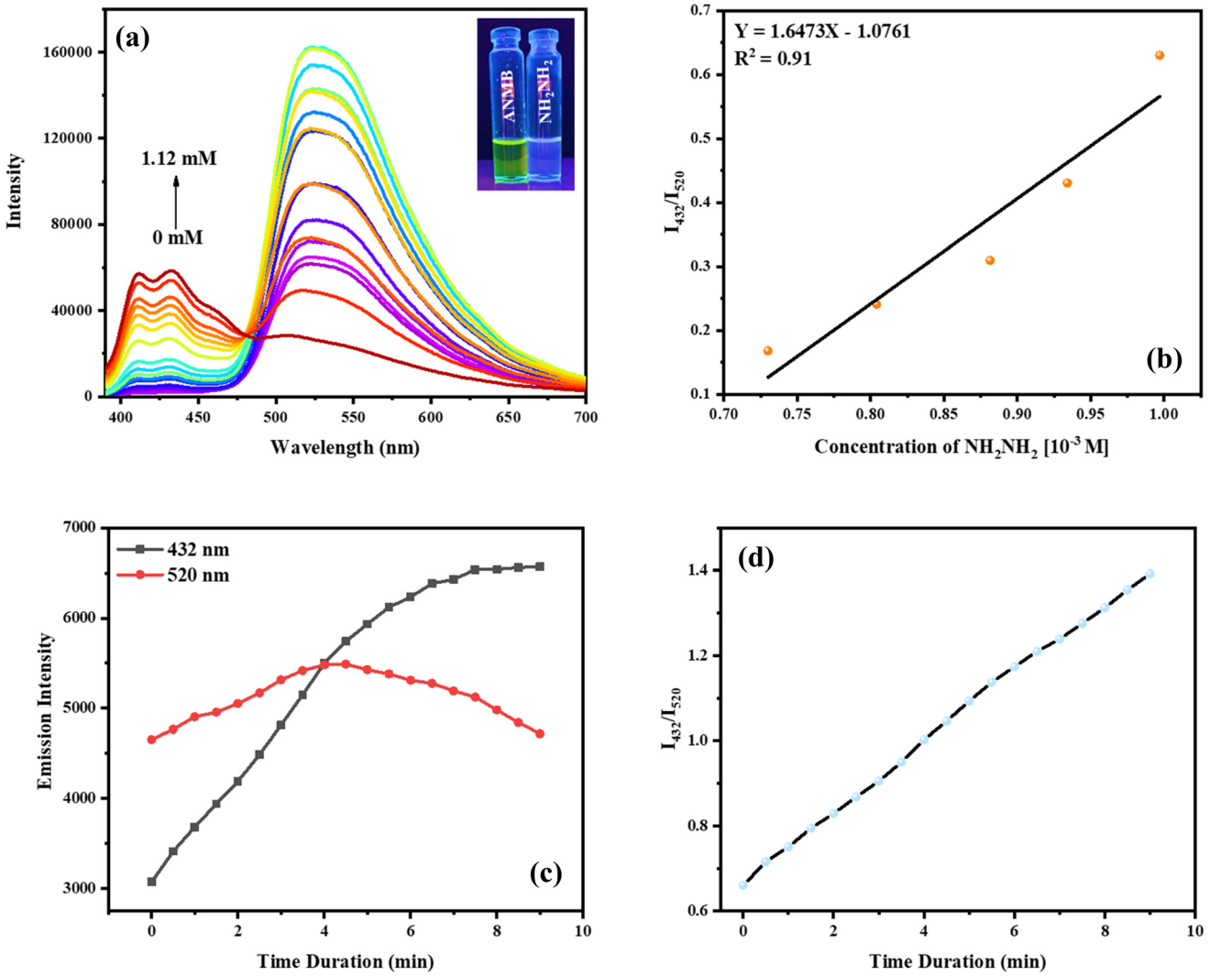

Fig. 10 (a) Emission titration spectra and (b) linear plot of ANMB with hydrazine. Time-dependent fluorescence response of the probe toward hydrazine: (c) variation of emission intensities at 432 and 520 nm with time after hydrazine addition; (d) corresponding ratiometric response (I_{432}/I_{520}) (ANMB (*c* = 36.5 μM); DMF/H_2O (9 : 1, v/v) at pH 7.4; λ_{ex} = 390 nm; slit width = 5 nm/5 nm; measured at room temperature).

the peaks at 411 nm and 432 nm displayed a brilliant blue fluorescence. These results indicated the full interaction of the **ANMB** and hydrazine (Scheme S2, SI), which was monitored using NMR (Fig. S7, SI). The LOD and LOQ were estimated using a linear plot of the emission intensity (I_{432}/I_{520}) *vs.* hydrazine concentration (Fig. 10b), and the values are 0.122 mM and 0.371 mM, respectively.

The temporal response of the probe toward hydrazine was investigated by monitoring the emission intensities at 432 and 520 nm as a function of time after hydrazine addition (Fig. 10c). The emission at 432 nm increases progressively, while the emission at 520 nm exhibits an initial rise, followed by a gradual decrease. In contrast, the ratiometric signal (I_{432}/I_{520}) displays a clear and monotonic increase with time (Fig. 10d), reaching a steady value within approximately 8–9 min and remaining stable thereafter with negligible variation, indicating a reaction-mediated sensing mechanism and demonstrating that the ratiometric response provides a reliable, time-resolved analytical signal suitable for quantitative hydrazine detection. A selectivity bar chart comparing the reaction of ANMB to hydrazine *versus* interferences has been provided (Fig. S8, SI) to assess the selectivity of ANMB towards hydrazine, which demonstrated that the ANMB exhibits high specificity for hydrazine over other tested species.

3.3.2.2. Fluorescent tag studies. Fluorescent tags were made from filter paper to develop a simple and reliable detection method for analyzing hydrazine in the solid state. As demonstrated in the image, the tags emitted lime green fluorescence when exposed to UV light (365 nm) but remained colorless under visible light. Various concentrations (0 mM to 15 mM) of hydrazine were introduced to the tags, and images were captured under UV light (365 nm) and visible light. The image revealed that with increasing the concentration of hydrazine, a color shift from lime green to blue fluorescence under UV light (365 nm) and from colorless to pale yellow under visible light is observed (Fig. 11). This color shift with varied hydrazine concentrations reveals an interaction between hydrazine and **ANMB**, which changes the photophysical properties of **ANMB**.

3.3.3. Molecular docking studies of ANMB. Molecular docking was conducted to promote an understanding of the potential biological activity of ANMB. Mus musculus opioid receptors (ORs), including muOR (μOR, PDB ID: 5C1M) and deltaOR (δOR, PDB ID: 4EJ4), and an M3 muscarinic acetylcholine receptor (PDB ID: 4U14) were explored using AutoDock Vina, as they majorly influence diarrheal due to their primary roles in regulating gastrointestinal (GI) motility and secretion. The interaction between μOR (PDB ID: 5C1M) and the ligands was evaluated by molecular docking studies. The structures indicate the free energy transition of ligand ANMB in its interactions with protein 4EJ4, DG = −7.8 kcal mol^{-1}, as shown in Fig. 12a and b. The 2D diagram shows that there is no conventional hydrogen-bonding interaction between ligand ANMB and the protein, whereas it formed a salt bridge interaction with the 112th glutamic acid residue *via* OE1/OE2 (residue atom) and the imine nitrogen (ligand). Additionally, pi-cation and pi-anion interactions with the 108th lysine, 112th glutamic acid, and 301st histidine residue, and various other hydrophobic interactions were observed in the A chain of protein 4EJ4. The structures indicate the free energy transition of ligand ANMB in its interactions with protein 4U14, DG = −8.1 kcal mol^{-1}, as shown in Fig. 12c and d. The 2D diagram shows that ligand ANMB forms one conventional hydrogen-bond interaction with the 225th leucine residue *via* the hydroxyl oxygen (ligand) and the backbone N–H or carbonyl oxygen (residue atom). Additionally, the pi-cation interaction with the 525th tryptophan residue and various other hydrophobic interactions were observed in the A chain of protein 4U14. The structures indicate the free energy transition of ligand ANMB in its interactions with protein 5C1M, DG = −7.1 kcal mol^{-1}, as shown in Fig. 12e and f. The 2D diagram shows that ligand ANMB forms three conventional hydrogen-bond interactions with the 220th threonine residue *via* hydroxyl oxygen (ligand) and the backbone N–H or carbonyl oxygen (residue atom) and the 222nd serine residue *via* carbonyl oxygen and imine nitrogen (ligand) with the backbone N–H or carbonyl oxygen (residue atom). Various other hydrophobic interactions were observed in the A chain of protein 5C1M. The summarized molecular interactions with amino acids of proteins (PDB ID: 4EJ4, 4U14, 5C1M) are represented in Table S5.

3.3.4. ADME properties of ANMB. The physicochemical characteristics of the powerful materials, including their water solubility, lipophilicity, bio-radar (for compounds that are tolerable when taken orally), drug similarity, and pharmacokinetics, were examined by *in silico* ADME study using SwissADME. The result is acceptable since **ANMB** does not violate Lipinski's, Ghose's, Veber's, Egan's or Muegge's rule of drug-likeness with zero violations. It also has a good bio-radar (Fig. S9, SI) and high gastrointestinal absorption property with blood–brain barrier (BBB) permeant property, making it orally administrable to humans. **ANMB** inhibits CYP (Cytochrome P50) enzymes other than CYP2D6 and CYP3A4, indicating a moderate risk of metabolic interference, and it does not act as a substrate

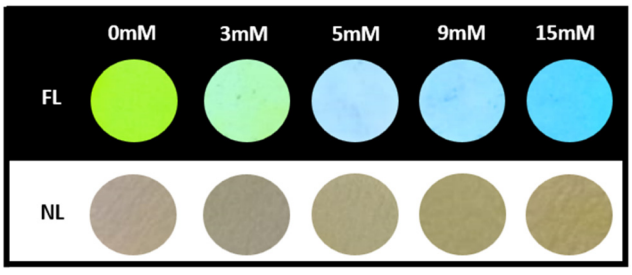

Fig. 11 Responsive behaviour of ANMB upon incremental addition of hydrazine in the solid state under UV light (365 nm) and visible light.

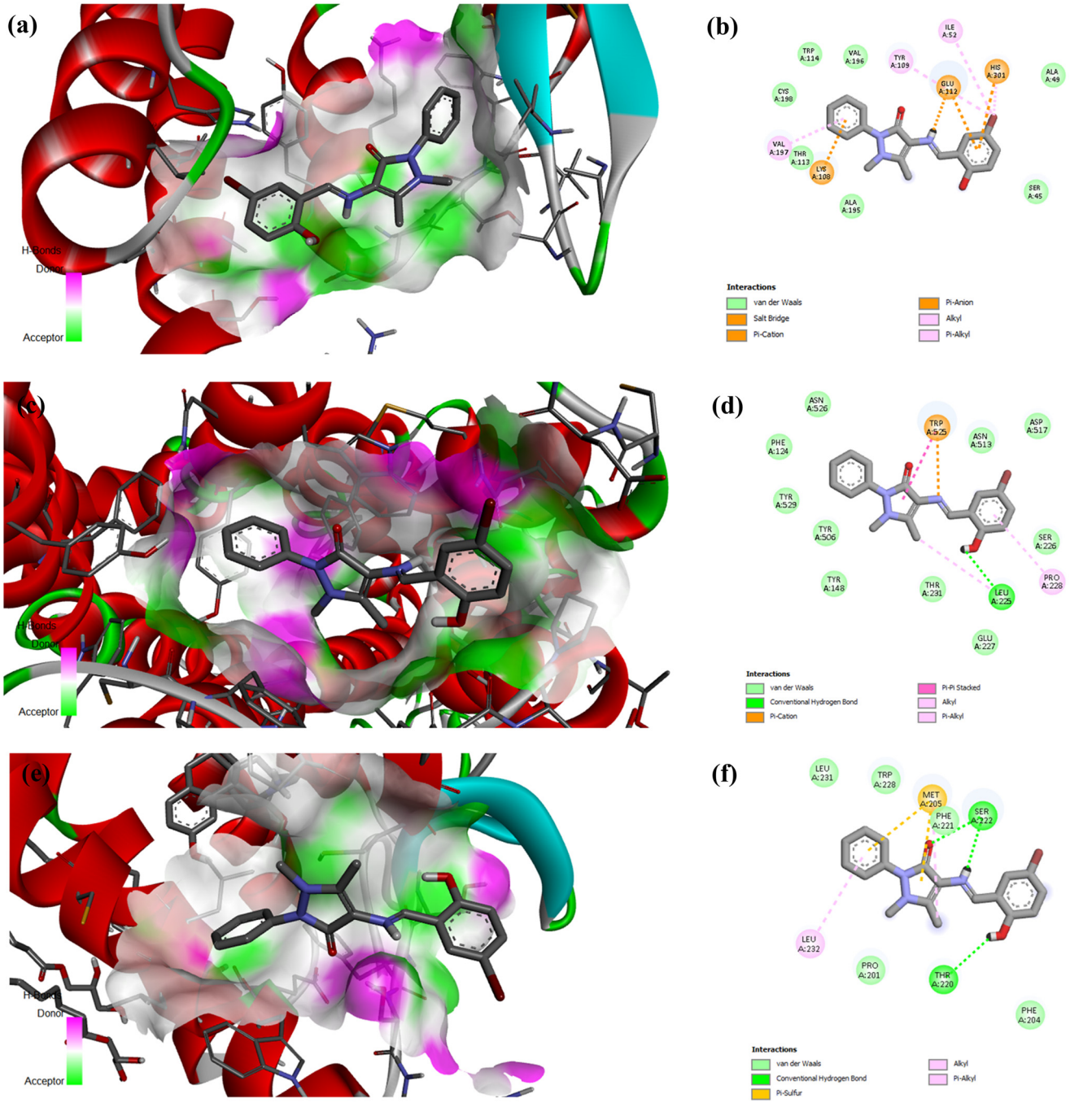

Fig. 12 (a) 3D and (b) 2D interactions of ANMB with protein 4EJ4. (c) 3D and (d) 2D interactions of ANMB with protein 4U14. (e) 3D and (f) 2D interactions of ANMB with protein 5C1M.

for P-glycoprotein, with a total polar surface area (TPSA) of 59.52 Å^2. Its strong log$P$ value of 3.49 and low log$S$ demonstrate its moderate solubility and drug-likeness, as represented in Table S3.

3.4 Real-time applications

3.4.1. Real water sample analysis. To assess the practical utility of **ANMB** for detecting Cu^{2+} and hydrazine, real-water sample experiments were conducted using river water, tap water, drinking water, and neem leaf extract. Since these environmental samples were not fully purified, trace amounts of metal ions or hydrazine could still be present, making detection more challenging. Each sample was first filtered using Whatman filter paper to remove particulate matter. Minimal interference was observed in the pretreated water samples, indicating negligible background effects on the fluorescence response of **ANMB**. Known concentrations of Cu^{2+} (10 μM) or hydrazine (0.5 mM) were then spiked into each sample. The fluorescence

Table 1 Determination of Cu^{2+} in different real water samples

Samples	Cu^{2+} spiked (μM)	Cu^{2+} recovered (μM)	Recovery (%)	RSD (%)
River water	10	10.17 ± 0.10	101.7	1.02
Tap water	10	9.73 ± 0.13	97.3	1.29
Drinking water	10	9.83 ± 0.08	98.3	0.78

Table 2 Determination of hydrazine in different real water samples

Samples	NH_2NH_2 spiked (mM)	NH_2NH_2 recovered (mM)	Recovery (%)	RSD (%)
Drinking water	0.5	0.484 ± 0.00513	96.94	1.06
Neem leaf extract	0.5	0.456 ± 0.00611	91.26	1.34

intensity was measured, and the corresponding analyte concentrations were determined using the previously established linear calibration curves. The recoveries for Cu^{2+} ranged from 97.3% to 101.7%, with relative standard deviations (RSDs) between 0.78% and 1.29% (Table 1). For hydrazine, the recoveries ranged from 91.26% to 96.94%, with RSDs of 1.06–1.34% (Table 2). The slightly lower recovery of hydrazine in neem leaf extract is likely due to the presence of naturally occurring plant metabolites, pigments, or other matrix components that can partially interfere with the reaction or fluorescence response of **ANMB**. Overall, these results indicate that **ANMB** provides accurate, reliable, and reproducible detection of Cu^{2+} and hydrazine in complex real-water and plant samples, demonstrating its practical applicability for environmental monitoring and biological matrices.

3.4.2. Live cell imaging of hydrazine in plants. To assess the applicability of **ANMB** in imaging hydrazine in the plants, chickpeas were initially allowed to sprout at ambient temperature. The germinated chickpea seeds were incubated for 2 hours with **ANMB** (10 mM) probe solutions and washed with a free solvent. Following incubation with **ANMB**, chickpea sprouts displayed strong green fluorescence under UV light (365 nm). Eventually, after treatment with hydrazine solution, the radicle and plumule parts of the sprouts showed bright blue fluorescence (Fig. 13a). This suggests that the accumulation of hydrazine in such parts of the sprout with lower concentrations can be imaged, as **ANMB** gets well absorbed in the plants and forms corresponding fluorophores on interaction with hydrazine. Stem sections of *Boerhavia diffusa L.* and *Bignonia magnifica* were used, and a change in the fluorescence emission from green to blue was observed in the presence of hydrazine (Fig. 13b–e). This indicates the additional applicability of **ANMB** in identifying hydrazine alterations in plant tissues, which extends its application scope beyond biological and environmental domains to plant kingdoms.

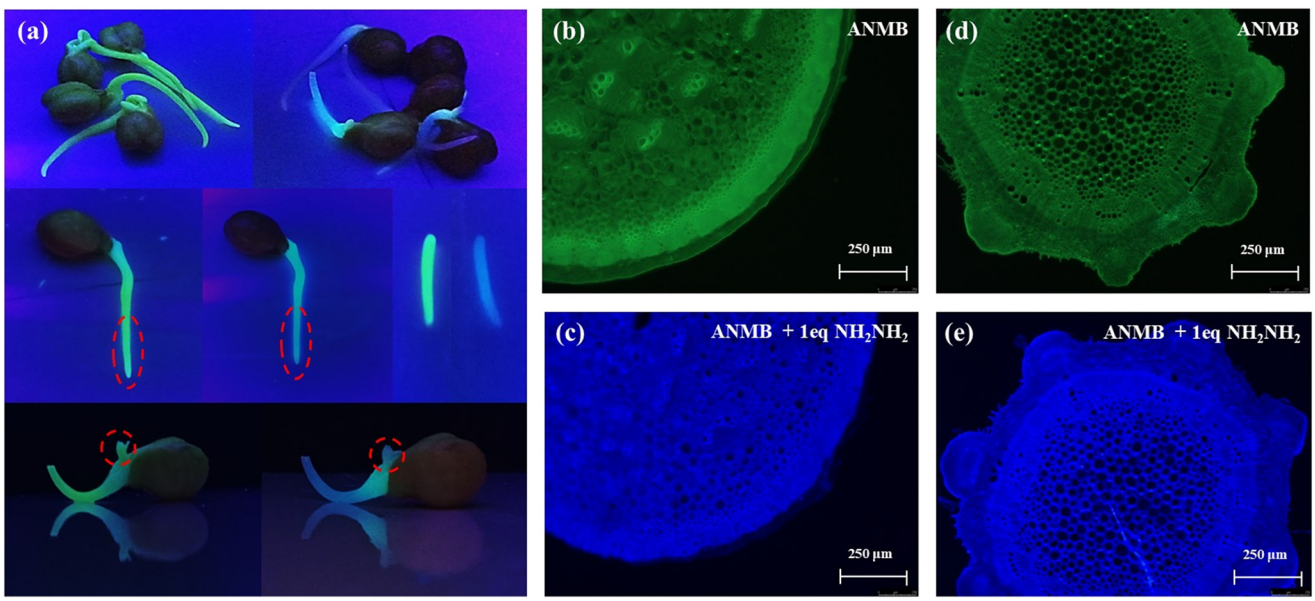

Fig. 13 (a) Imaging hydrazine in chickpea sprouts. Plant sample (*Boerhavia diffusa L.*) treated with (b) ANMB and (c) ANMB + 1 eq of NH_2NH_2. Plant sample (*Bignonia magnifica*) treated with (d) ANMB and (e) ANMB + 1 eq of NH_2NH_2.

4. Conclusion

In this study, we developed and characterized a novel dual-state emissive (DSE) organic luminogen, **ANMB**, incorporating an excited-state intramolecular proton transfer (ESIPT) mechanism. **ANMB** displayed an exceptional Stokes shift—109 nm in solution and 155 nm in the solid state—providing strong evidence of its potential as a multifunctional sensor. Its structural design enabled both solution-phase and solid-state emission, which is a critical requirement for practical sensing platforms, especially for biological and environmental diagnostics. **ANMB** exhibited pronounced quenching upon chelation with Cu^{2+} ions, indicating high sensitivity and selectivity for metal-ion detection. This quenching effect served as a basis for fluorescence recovery experiments, where the probe demonstrated enantioselective recognition of amino alcohols. Notably, the *S*-enantiomer led to a single emission peak, while the *R*-enantiomer resulted in dual emission peaks, demonstrating **ANMB**'s capacity to distinguish chiral molecules, which is of great importance in pharmaceutical and biochemical fields. Further, **ANMB** proved to be an effective and selective chemosensor for hydrazine. Its interaction with hydrazine induced a clear spectral shift with new emission peaks at 411 nm and 432 nm, corresponding to a visible change from green to blue fluorescence. In addition to its sensing capabilities, *in silico* docking studies suggested a potential therapeutic application of **ANMB** in targeting biological pathways relevant to diarrheal diseases. This highlights the compound's promise in not only diagnostic domains but also therapeutic domains, warranting further biological and pharmacological investigations. Taken together, this work underscores the power of integrating DSE and ESIPT mechanisms into organic luminogens to create highly sensitive, selective, and versatile materials for multifunctional applications. **ANMB** represents a valuable advancement in the field of luminescent materials, with prospective utility in chiral sensing, environmental monitoring, toxic-substance detection, and potential therapy development.

Conflicts of interest

There are no conflicts to declare.

Data availability

All the data supporting the findings of this study are included as text, figures, and tables. Other supporting data are available in the supplementary data. Supplementary information (SI) is available. See DOI: https://doi.org/10.1039/d5sd00214a.

Acknowledgements

The authors would like to thank Christ University for constant encouragement and support. The authors extend their appreciation to the Centre for Research at CHRIST University for funding this work through seed fund money under grant number CU-ORS-SM-24/12.

References

1 A. Mondal, E. Ahmmed, B. Ball and P. Chattopadhyay, *ChemistrySelect*, 2022, **7**, e202103857, DOI: 10.1002/slct.202103857.
2 A. Venkatesan, A. Cherian and A. Nizam, *Analyst*, 2025, **150**, 5124–5141, DOI: 10.1039/D5AN01012H.
3 G. Vargas-Nadal, M. Köber, A. Nsamela, F. Terenziani, C. Sissa, S. Pescina, F. Sonvico, A. M. Gazzali, H. A. Wahab, L. Grisanti and M. E. Olivera, *Pharmaceutics*, 2022, **14**, 2498, DOI: 10.3390/pharmaceutics14112498.
4 X. Tian, L. C. Murfin, L. Wu, S. E. Lewis and T. D. James, *Chem. Sci.*, 2021, **12**, 3406–3426, DOI: 10.1039/d0sc06928k.
5 J. Kim, J. H. Oh and D. Kim, *Org. Biomol. Chem.*, 2021, **19**, 933–946, DOI: 10.1039/d0ob02387f.
6 T. Stoerkler, T. Pariat, A. Laurent, D. Jacquemin, G. Ulrich and J. Massue, *Molecules*, 2022, **27**, 2443, DOI: 10.3390/molecules27082443.
7 M. Jia, Y. Ren, S. Xiong, S. Li, P. Wang and C. Zhao, *Spectrochim. Acta, Part A*, 2025, **346**, 126942, DOI: 10.1016/j.saa.2025.126942.
8 Y. Ren, M. Jia, S. Xiong, C. Pu, P. Wang and Y. An, *Spectrochim. Acta, Part A*, 2025, **216**, 114732, DOI: 10.1016/j.microc.2025.114732.
9 J. Yin, Y. Kwon, D. Kim, D. Lee, G. Kim, Y. Hu, J. H. Ryu and J. Yoon, *J. Am. Chem. Soc.*, 2014, **136**, 5351–5358, DOI: 10.1021/ja412628z.
10 H. Tian Jr, A. C. Sedgwick, H. H. Han, S. Sen, G. R. Chen, Y. Zang, J. L. Sessler, T. D. James, J. Li and X. P. He, *Coord. Chem. Rev.*, 2021, **427**, 213577, DOI: 10.1016/j.ccr.2020.213577.
11 M. Gao, F. Yu, C. Lv, J. Choo and L. Chen, *Chem. Soc. Rev.*, 2017, **46**, 2237–2271, DOI: 10.1039/c6cs00908e.
12 Y. Hong, W. Y. J. Lam and B. Z. Tang, *Chem. Commun.*, 2009, 4332–4353, DOI: 10.1039/b904665h.
13 D. C. Magri, *Coord. Chem. Rev.*, 2021, **426**, 213598, DOI: 10.1016/j.ccr.2020.213598.
14 X. F. Li, W. Zhou, Y. C. Liu, M. Hou, G. L. Feng, Y. M. Ji, Y. Zhang and G. W. Xing, *Chem. Commun.*, 2022, **58**, 11547–11550, DOI: 10.1039/D2CC04760H.
15 A. Syed, H. Renuka, A. Mohitkar, R. Pallepogu, M. S. K. Challa, S. Goel and S. Jayanty, *Mater. Adv.*, 2022, **3**, 3151–3164, DOI: 10.1039/d1ma00778e.
16 M. Shimizu and T. Hiyama, *Chem. – Asian J.*, 2010, **5**, 1516–1531, DOI: 10.1002/asia.200900727.
17 J. Gierschner, J. Shi, B. Milián-medina, D. Roca-sanjuán, S. Varghese and S. Y. Park, *Adv. Opt. Mater.*, 2021, **9**, 2002251, DOI: 10.1002/adom.202002251.
18 M. Gsänger, D. Bialas, L. Huang, M. Stolte and F. Würthner, *Adv. Mater.*, 2016, **28**, 3615–3645, DOI: 10.1002/adma.201505440.
19 G. Chen, W. Li, T. Zhou, Q. Peng, D. Zhai, H. Li, W. Z. Yuan, Y. Zhang and B. Z. Tang, *Adv. Mater.*, 2015, **27**, 4496–4501, DOI: 10.1002/adma.201501981.

20 X. Li, M. Li, Y. Chen, G. Qiao, Q. Liu, Z. Zhou, W. Liu and Q. Wang, *Chem. Eng. J.*, 2021, **415**, 128975, DOI: 10.1016/j.cej.2021.128975.
21 T. Pariat, M. Munch, M. Durko-Maciag, J. Mysliwiec, P. Retailleau, P. M. Verite, D. Jacquemin, J. Massue and G. Ulrich, *Chem. – Eur. J.*, 2021, **27**(10), 3483–3495, DOI: 10.1002/chem.202004767.
22 F. Joy, A. V. J. Devasia and A. Nizam, *Appl. Spectrosc. Rev.*, 2024, **59**, 959–988, DOI: 10.1080/05704928.2023.2276925.
23 F. Joy, A. V. J. Devasia and A. Nizam, *Supramol. Chem.*, 2024, 1–13, DOI: 10.1080/10610278.2024.2406269.
24 F. Joy, J. Devasia, Y. Nair and A. Nizam, *Food. Chem.*, 2023, **427**, 136643, DOI: 10.1016/j.foodchem.2023.136643.
25 B. V. N. Sahithi and V. V. Lakshmaiah, *RSC Adv.*, 2025, **15**, 28721–28729, DOI: 10.1039/D5RA04728E.
26 A. Venkatesan, A. Nizam, A. R. Cherian, R. Patel, J. Xavier, P. K R, H. R and N. G, *RSC Adv.*, 2025, **15**, 32638–32653, DOI: 10.1039/D5RA05696A.
27 US-EPA and U.S.-E.P.A., *National Primary Drinking Water Regulations*, US-EPA, 2009.